Applied Acoustics 205 (2023) 109256

Contents lists available at ScienceDirect

Applied Acoustics

journal homepage: www.elsevier.com/locate/apacoust

A simplified semi-empirical model for long-range low-frequency noise propagation in the turbulent atmosphere

Tianshu Zhang *, Steven A.E. Miller

University of Florida, Gainesville 32611, FL, USA

ARTICLE INFO

Article history:
Received 28 August 2022
Received in revised form 21 December 2022
Accepted 1 February 2023

Keywords:
Acoustic-turbulent interaction
Wind tunnel test

ABSTRACT

We present a semi-empirical long-range low-frequency acoustic propagation model, which accounts for atmospheric turbulence. Ostashev and Wilson's scattering model is combined with a ray-theory based refraction model to account for turbulent scattering and refraction via a turbulent absorption coefficient. The coefficient is ascertained via integration of scattered energy. The model is formulated, calibrated, and validated via corresponding experiments conducted within the National Science Foundation Boundary Layer Wind Tunnel. The predictions of the newly proposed 'bridging model' match the wind tunnel experimental data with an average error of 11.9%. Example predictions are shown to quantify the effect of turbulent kinetic energy and turbulent integral length scale on long-range infrasound propagation. To demonstrate the approach, we present predictions of the propagation of noise from a tornado and a nonlinear wave.

1. Introduction

Acoustic waves are scattered by turbulence. This effect must be accounted for to make accurate predictions of long-range acoustic propagation in the atmosphere [1]. This is especially true at lower altitudes in the atmosphere [2]. Ostashev and Wilson [3] developed a model to account for the scattering of acoustic waves through an inhomogeneous anisotropic turbulent field, which includes fluctuations of velocity and temperature. We introduce a modification of Ostashev and Wilson[3]'s model. This modification focuses on the effects of large-scale turbulent structures in the forward scattering direction within the altitude range of 0 to 20 km.

Investigators have studied turbulent scattering using different approaches, including parabolic equation methods and statistical scattering models. The parabolic equation method for wave propagation, such as Khokhlov Zabolotskaya Kuznetsov (KZK) equation [4,5], is a classic approach to capture turbulent effects. Blanc-Benon et al. [6] implemented a model numerically with the KZK propagation equation and analyzed their results with experimental data. Experimental data is also employed to analyze the turbulent effects on sonic boom propagation. Lipkens [7] validated the statistical model of Pierce [8] with sonic boom experiments by comparing the rise time of the mean waveform to the rise time altered by turbulence. The plane-wave assumption is employed for sonic boom propagation, especially near the ground, and the scattered waves exhibit 'folding' effects. Piacsek [9] investigated and validated the folding and focusing effect of the turbulence on sonic boom propagation. Stout et al. [10] showed how turbulence could affect an N-wave by analyzing the perceived level (PL), and the turbulent effects on indoor sonic boom annoyance predictor metrics [11]. For long-range propagation, the plane wave assumption is not valid. The performance of these statistical models for long-range low-frequency propagation is not as satisfactory as for sonic boom propagation. The model of Goldreich and Kumar [12] simplified the turbulent scattering model by using the mass and velocity fluctuations of the turbulent structures to evaluate the turbulent scattering effect. Brown and Clifford [13] developed a turbulent scattering attenuation model by using the sound beam approach, which also relates the scattering intensity to the turbulent kinetic energy and turbulent length scale.

Besides the parabolic equation methods and statistical models, the coefficient predicted by Lighthill's model [14] revealed that acoustic-turbulent attenuation can be related to turbulent kinetic energy and integral length scale. In 1967, Tatarski [15] presented his turbulent scattering model, which was able to predict the directional scattering via a turbulence spectrum. Later, Ostashev and Wilson [3] improved the Tatarski [15]'s model by correcting the coefficient and included the effect of humidity. However, in Ostashev and Wilson [3], the predicted cross-section for the near-zero

* Corresponding author.

https://doi.org/10.1016/j.apacoust.2023.109256
0003-682X/

scattering angle is invalid because of the appearance of a singularity. To overcome this, Muhsin et al. [16] numerically investigated the small-angle scattering effects via a finite-difference time-domain approach. With the inhomogeneity of temperature, [16] obtained a non-zero cross-section for the zero-degree scattering angle. Our model leverages Ostashev and Wilson [3]'s model and incorporates a turbulent refraction model to account for the large-scale turbulent effects.

The present model is based on Ostashev and Wilson [3]'s model, and the new model is modified to account for turbulent scattering and refraction in a simplified way. The refraction caused by the large-scale turbulence is included in the new model using classic refraction ray theory and a decomposed turbulent field. We performed acoustic propagation experiments within the University of Florida Boundary Layer Wind Tunnel (UFBLWT). The new model is validated with this unique dataset.

The generalized Burgers' equation [17,18] can capture the effects of absorption, dispersion, and nonlinearity. If coupled with acoustic ray tracing, the refraction can also be included in this propagation method. This weakly nonlinear propagation method is widely used in long-range propagation prediction, such as the Misty Picture study by Scott et al. [19]. However, the generalized Burgers' equation is unable to predict turbulent effects due to its spatially one-dimensional nature. By implementing the presently proposed turbulent scattering model into a validated generalized Burgers' equation solver, we provide a new propagation method with an ability to capture scattering of turbulence. We also investigate turbulent attenuation effects for two broadband signals, and numerically investigate the model's behavior by varying the turbulent kinetic energy (TKE) and length scale, L_v. This new model also has potential applications for propagating volcano eruption infrasound, explosion infrasound, and aircraft take-off noise.

The rest of the paper is organized as follows: Section 2 introduces the mathematical derivation of our model; Section 3 discusses the wind tunnel validation of the model; Section 4 presents demonstration cases of the model application for long-range propagation. Finally, Section 5 presents the summary and conclusion.

2. Methodology

In this section, Ostashev's model, the bridging model, and the model implementation in the generalized Burgers' equation are introduced in three subsections. To model wave turbulence interaction that occurs during long-range propagation, a bridging model is proposed that combines Ostashev and Wilson's model (Ostashev's model for short) [3] and traditional linear acoustic refraction. The long-range low-frequency propagation assumption, $R \gg \lambda$, is made, where R is the propagation distance and λ is the wavelength of the acoustic wave. Acoustic frequencies studied are between 0.10 Hz to 1000 Hz, which correspond to frequencies of interest for natural phenomena within the atmosphere. A turbulent attenuation coefficient, α_t, is generated by the bridging model, and this coefficient is integrated into the generalized Burgers' equation.

2.1. Ostashev and Wilson's Turbulent Scattering Model

Before introducing a new turbulent attenuation coefficient, α_t, we examine the Ostashev and Wilson [3]'s turbulent scattering model. Directional turbulent scattering was investigated by Tatarski [15] and Ostashev and Wilson [3] improved Tatarski's model by using a Helmholtz-type equation (Eqn. 6.91 in [3]). The scattering field is (see Eqn. 6.110 in [3])

$$< I_s >= \frac{2\pi k^4 I_0 \mathbf{n}}{R^2}\left[\frac{\beta^2(\theta)\Phi_T(\mathbf{q})}{4T_0^2}+\frac{\beta(\theta)\eta(\theta)\Phi_{CT}(\mathbf{q})}{2T_0}+\frac{\eta^2(\theta)\Phi_C(\mathbf{q})}{4}+\frac{\cos^2\theta n_{0,i}n_{0,j}\Phi_{ij}(\mathbf{q})}{c^2}\right], \tag{1}$$

where the $< I_s >$ is the mean acoustic intensity of the scattered field, k is the wave number of the acoustic wave, coordinates' origin is located at the scattering location, $\mathbf{n}$ is the direction of the scattered wave, I_0 is the intensity of the incident acoustic wave, R is the distance from the scattering location to the observer, β and η are the construction parameters defined by Eqn. 6.67 of [3], θ is the scattering angle, $\mathbf{q}$ is the scattering vector, and $\Phi_T, \Phi_{CT}, \Phi_C$, and Φ_{ij} are the spectra of temperature, humidity-temperature, humidity, and velocity fluctuations, respectively. Then Eqn. 1 can be simplified and represented by the cross-section σ as

$$\begin{aligned}\sigma(\theta) &= \sigma(\mathbf{n}-\mathbf{n_0}) \\ &= 2\pi k^4\left[\frac{\beta^2(\theta)\Phi_T(\mathbf{q})}{4T_0^2}+\frac{\beta(\theta)\eta(\theta)\Phi_{CT}(\mathbf{q})}{2T_0}+\frac{\eta^2(\theta)\Phi_C(\mathbf{q})}{4}+\frac{\cos^2\theta\cot^2(\theta/2)E(\mathbf{q})}{16\pi k^2\bar{c}^2}\right],\end{aligned} \tag{2}$$

where $\sigma(\theta)$ is the scattering cross-section and is

$$\sigma(\theta) = \frac{I_s(\theta)R^2}{I_0 V}. \tag{3}$$

The referenced cross-section is on a per unit volume basis. More details about Ostashev's model are available in Ostashev and Wilson [3].

The temperature and humidity fluctuations are mainly induced by the ground fluxes, which are most prevalent below the altitude of 100 m [3]. For our investigation, the altitude range is from 0 to 20 km, and the ground fluxes only affect a small portion (0.5%) of the altitude range, thus the fluctuations of the first three terms in Eqn. 2 are negligible in the rest of the model derivation. For future development, the temperature and humidity fluctuations may also be integrated into the propagation equation. Thus, in the following investigation, only the fourth term on the right hand side is retained to account for the velocity inhomogeneity, and this term is named the turbulent cross-section σ_E as

$$\sigma_E(\theta) = 2\pi k^4\left[\frac{\cos^2\theta\cot^2(\theta)E(2k\ \sin\frac{\theta}{2})}{16\pi k^2 c^2}\right], \tag{4}$$

where $E(\kappa)$ is the turbulent velocity spectrum. Here, the von Kármán spectrum is used as it is commonly adapted for long-range prediction. The velocity spectrum is modeled as

$$E(\kappa) = \frac{55\Gamma(5/6)}{9\pi^{\frac{1}{2}}\Gamma(1/3)}\frac{\sigma_v^2\kappa^4 L_v^5}{\left(1+\kappa^2 L_v^2\right)^{17/6}}, \tag{5}$$

where $\kappa = 2k\sin\frac{\theta}{2}$ is the scattering wave number, Γ is the gamma function, and σ_v is the variance of the fluctuating velocity. Because our goal is to predict the scattered acoustic energy, the total scattering cross-section is needed. It is found from the integration of the entire turbulent sphere of scattering as

$$\sigma_{E,\text{tot}} = \int_0^{2\pi}\int_0^{\pi}\sigma_E(\theta)\sin(\theta)d\theta d\phi, \tag{6}$$

where subscript tot denotes total. In the following section, we will describe the approach to obtain the scattering energy loss by using the total cross section.

2.2. Turbulent Refraction and Bridging Model

In the previous model formulation, small values of θ may cause a singularity and invalidate the predicted cross-section. As θ

approaches zero, $\kappa = 2k\sin\frac{\theta}{2}$ also reaches zero, indicating that the scattering near the forward propagation direction is caused by large (or extremely large) scale turbulence. However, when the turbulent length scale is larger than the acoustic wavelength, turbulence is believed to contribute to acoustic-turbulent interaction instead of scattering in terms of wave length. Here, we treat turbulent refraction as a statistical concept, which is different from the traditional acoustic refraction concept. A detailed definition of turbulent refraction is presented in the following discussion as a new acoustic-turbulent interaction model.

The new model is presented via Fig. 1. In Fig. 1, a right-running incident wave arrives with the condition $R \gg \lambda$ (where R is assumed larger than 10 km), and the wave is represented by the incident ray tubes at t. Acoustic-turbulent interaction occurs during the time span between t and $t + \delta t$. The blue sphere represents a turbulent eddy. Θ_s is the scattering angle, $\mathbf{K_r}$ is the turbulent refraction wave vector, and Θ_r is the turbulent refraction angle. $d\sigma_E$ is the turbulent scattering cross-section discussed in the previous subsection. The other parameters will be presented next.

To capture the refraction caused by the turbulence, the geodisc elements technique of ray theory [17,20] is employed to represent the ray tube and to construct the convective volume. The governing equation [21] for the geodisc element $\mathbf{X_{p_i}}$ is

$$\begin{aligned}\frac{d\mathbf{X_{p_i}}}{dt} &= \frac{\partial}{\partial p_i}\left(\bar{c}(\mathbf{X},t)\mathbf{N} + v_0(\mathbf{X},t)\right)\\ &= \bar{c}\frac{\partial \mathbf{N}}{\partial p_i} + (\mathbf{X_{p_i}}\cdot\nabla\bar{c})\mathbf{N} + (\mathbf{X_{p_i}}\cdot\nabla)\mathbf{v_0},\end{aligned} \tag{7}$$

where $\bar{c}$ is the time-averaged speed of sound, v_0 is the mean atmospheric wind speed, and the subscript $\mathbf{p_i}$ represents the local coordinate system at the wave front.

The first step is the decomposition of the velocity field as $\mathbf{v_0} = \overline{\mathbf{v_0}} + \mathbf{v_0'}$, where $\overline{\mathbf{v_0}}$ is the mean velocity and $\mathbf{v_0'}$ is the fluctuating component. Then the governing equation for geodisc elements $\mathbf{X_{p_i}}$ are

$$\begin{aligned}\frac{d\mathbf{X_{p_i}}}{dt} &= \frac{d\overline{\mathbf{X}}_{\mathbf{p_i}}}{dt} + \frac{d\mathbf{X'_{p_i}}}{dt}\\ &= \bar{c}\frac{\partial \mathbf{N}}{\partial p_i} + (\mathbf{X_{p_i}}\cdot\nabla\bar{c})\mathbf{N} + (\mathbf{X_{p_i}}\cdot\nabla)(\overline{\mathbf{v_0}} + \mathbf{v_0'}).\end{aligned} \tag{8}$$

The additional $(\mathbf{X_{p_i}}\cdot\nabla)\mathbf{v_0'}$ term is the fluctuating geodisc element generated by the turbulent refraction. Unlike the governing equation of the geodisc element $\mathbf{X_{p_i}}$ in Eqn. 7, the $\mathbf{X'_{p_i}}$ is generated along the ray path and is independent relative to the value at previous times. Thus, the term $\frac{d\mathbf{X'_{p_i}}}{dt}$ can be interpreted as the generation rate of a turbulent-refraction geodisc element. In Gainville [21]'s research, the convection volume is defined as

$$v = \frac{|\mathbf{X_1}\wedge\mathbf{X_2}|}{|\mathbf{K}|} = \frac{|\mathbf{X_1}\wedge\mathbf{X_2}|\cdot\lambda}{2\pi}, \tag{9}$$

where $\mathbf{X_1}$ and $\mathbf{X_2}$ are corresponding geodisc elements, which are perpendicular to the wave vector. The geodisc elements $\mathbf{X_1}$ and $\mathbf{X_2}$ are presented in Fig. 1 in the incident ray tube at t. Since the magnitude of the wave vector $\mathbf{K_r}$ is the same as the incident wave vector $\mathbf{K}$, the turbulent refracted convective volume is

$$v' = \frac{|\mathbf{X'_1}\wedge\mathbf{X'_2}|}{|\mathbf{K_r}|} = \frac{|\mathbf{X'_1}\wedge\mathbf{X'_2}|}{|\mathbf{K}|} = \frac{|\mathbf{X'_1}\wedge\mathbf{X'_2}|\cdot\lambda}{2\pi}. \tag{10}$$

The v' is also represented in Fig. 1 by the sub ray tube in the right lower corner. The sub ray tube is produced by the generation of $\mathbf{X'_1}$ and $\mathbf{X'_2}$. If the field is represented by locally isotropic turbulence, the direction of the refracted wave vector $\mathbf{K_r}$ deviates from the mean incident wave vector $\overline{\mathbf{K}}$.

The turbulent refracted convective volume v' is required to ascertain the intensity of refracted waves. In Eqn. 10, $\mathbf{X'_1}$ and $\mathbf{X'_2}$ represent the value of $\frac{d\mathbf{X'_1}}{dt}$ and $\frac{d\mathbf{X'_2}}{dt}$, respectively, which are the generation rates of the geodisc elements for the sub ray tube. The governing equation of $\mathbf{X'_i}$ is obtained from Eqn. 8 as

$$\mathbf{X'_i} = \frac{d\mathbf{X'_{p_i}}}{dt} = (\mathbf{X_{p_i}}\cdot\nabla)\mathbf{v'_0}. \tag{11}$$

Because the magnitude of the incident wave vector is identical to the refracted wave vector, its influence on the value of the convective volume can be ignored. Thus Eqn. 11 can be expanded as

$$\begin{aligned}X'_{1,j} &= \tfrac{1}{2}X_{1,i}\left(\frac{\partial v'_{0,i}}{\partial p_j} + \frac{\partial v'_{0,j}}{\partial p_i}\right);\\ X'_{2,j} &= \tfrac{1}{2}X_{2,i}\left(\frac{\partial v'_{0,i}}{\partial p_j} + \frac{\partial v'_{0,j}}{\partial p_i}\right).\end{aligned} \tag{12}$$

Then the refracted convective volume is obtained by inserting Eqn. 12 into Eqn. 10 as

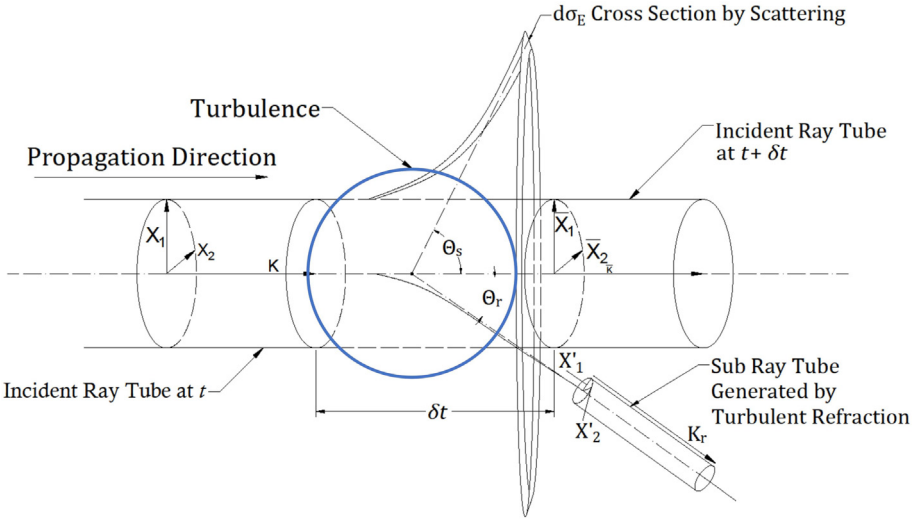

Fig. 1. Concept of the bridging model.

$$v' = \frac{\lambda}{8\pi} X_{1,i} X_{2,i} \overline{\left(\frac{\partial v'_{0,i}}{\partial p_j} + \frac{\partial v'_{0,j}}{\partial p_i}\right)^2} \cos(\mathbf{X_1}, \mathbf{X_2}) = \frac{\lambda}{8\pi} X_{1,i} X_{2,i} \overline{s_{ij} s_{ij}} \cos(\mathbf{X_1}, \mathbf{X_2}). \tag{13}$$

To ascertain the cross-section from the refracted convective volume, the turbulent refraction cross-section σ_r is defined as

$$\sigma_r = \frac{v'}{v} = \frac{\overline{s_{ij} s_{ij}}}{4} \sim \frac{\sigma_v^2}{\lambda_T^2}, \tag{14}$$

where the σ_r is defined as the ratio of refracted convective volume to the mean convective volume, the term $\overline{s_{ij} s_{ij}}$ represents fluctuating strain rate, σ_v is the turbulent velocity variance, and λ_T is the Taylor microscale [22]. Therefore, the relation between the turbulent wave number and the fluctuating strain rate is employed [23] as

$$\overline{s_{ij} s_{ij}} = \frac{\epsilon}{2\nu} = \int_0^\infty k^2 E(k) dk. \tag{15}$$

For low-frequency waves, the large-scale turbulence has the greatest effect on turbulent refraction. Thus, only the turbulence with length scale larger than L_v is used within $\overline{s_{ij} s_{ij}}$, then σ_r is

$$\sigma_r = \frac{v'}{v} \sim \frac{\sigma_v^2}{\lambda_T^2} \frac{\int_0^{2\pi/L_v} k^2 E(k) dk}{\int_0^\infty k^2 E(k) dk}. \tag{16}$$

Here, we define the variable C_E as $\left(\int_0^{2\pi/L_v} k^2 E(k) dk\right) / \left(\int_0^\infty k^2 E(k) dk\right)$, which ranges from approximately 10^{-6} to 10^{-4} within the von Kármán spectrum. Thus, σ_r can also be represented as $\sigma_r = C_F \sigma_v^2 / L_v^2$, where $C_F = L_v^2 C_E / \lambda_T^2$. Now the σ_r is expressed as a function of the turbulent kinetic energy and integral length scale, with a variable C_E. The ratio between the Taylor length scale and integral length is $15^{1/2} Re_l^{-0.5}$.

Unlike the scattering term of Eqn. 3, σ_r is no longer a function with respect to the scattering angle because of the integration of $k^2 E(k)$ from 0 to $2\pi/L_v$ in Eqn. 16. Thus, we require a model function to bridge the refraction cross-section, σ_r, with the directional scattering cross-section, σ_E. Since the refraction model is only valid at low scattering angles (where $k \sin(\theta/2) < 2\pi/L_v$), a sine function is selected with σ_r as

$$\sigma_{eff}(\theta) = \max[\sigma_E(\theta)] - \frac{A}{\sigma_r} \left[\sin\left(\frac{\pi k_r L_v}{2} - \frac{\pi}{2}\right) - 1\right], \tag{17}$$

where A is a constant coefficient to be determined, $k_r = 2k \sin\frac{\theta}{2}$, and $k_r \in \left(0, \frac{2\pi}{L_v}\right)$. By applying this bridging function (inspired by Blackstock [24]), the turbulent refraction can be represented by the area below the sine curve and can be adjusted by the parameters in Eqn. 17. Finally, we obtain the expression for the effective total cross-section as

$$\sigma_{tot} = \sigma_{eff} + \int_0^{2\pi} \int_{2\arcsin\left(\frac{\pi}{kL_v}\right)}^{\pi} \sigma_E(\theta) \sin(\theta) d\theta d\phi, \tag{18}$$

An example plot of the bridging model is shown in Fig. 2. In this figure, the acoustic signal is a 10 Hz plane wave impacting on a turbulent structure with TKE of 0.2 m^2/s^2, while the L_v varies as 2 m, 16 m, and 96 m.

Fig. 2 shows the difference between the new model and Ostashev [3]'s model. Turbulent refraction is considered in the new model to account for the acoustic-turbulent interaction near zero scattering angle.

To implement the bridging model into the generalized Burgers' propagation equation, we transfer the total cross-section into a turbulent attenuation coefficient. The total cross-section is the ratio of the scattered energy to the incident energy, which can be expressed as

$$\sigma_{tot} = \frac{I_s}{I_0} = \frac{p_s^2}{p_0^2} = 1 - \frac{p_t^2}{p_0^2}, \tag{19}$$

where p_s is the scattering acoustic pressure and p_t is the transmitted acoustic pressure. Since the turbulent attenuation coefficient is acting similarly to the atmospheric absorption coefficient, we introduce the atmospheric absorption first. By assuming a time-harmonic waveform, the wave equation solution can be expressed as Blackstock [25]

$$p(\omega) = p_0 e^{-\alpha(\omega) r} e^{j(\omega t - \beta(\omega) r)}, \tag{20}$$

where r is the propagation distance, β is the wavenumber, α is the atmospheric absorption coefficient, and ω is the frequency. For the turbulent attenuation, we have

$$\frac{p_t(\omega)}{p_o(\omega)} = e^{-\alpha_t(\omega) r} e^{j(\omega t - \beta(\omega) r)}. \tag{21}$$

We now have the relation between the total cross-section and the attenuation coefficient as

$$\alpha_t = -\frac{1}{r} \ln\left[\frac{p_t}{p_0}\right] = \frac{1}{r} \ln\sqrt{1 - \sigma_{tot}}. \tag{22}$$

The unit of obtained α_t is nepers/m, which can be translate to the dB/m by a scale factor of 8.686.

2.3. Modified Burgers' Equation Propagation Model

We now examine how the modified model is integrated with Burgers' equation. The governing equation of the acoustic pressure is (see [21])

$$\frac{\partial p}{\partial t} = \delta \frac{\partial^2 p}{\partial \xi^2} + Bp \frac{\partial p}{\partial \xi} + \sum_\zeta (\Delta c)_\zeta \frac{\partial p_\zeta}{\partial \xi}, \tag{23}$$

where p is the acoustic pressure, K is the wave number, ξ is the length along the ray, δ is the thermal viscosity, and Δc_ζ is the difference of the speed of sound between component ζ and the ambient speed of sound. The nonlinear coefficient B is

$$B = \left(\frac{1+\gamma}{2}\right)\left(\frac{1}{\rho_0 c_0}\right). \tag{24}$$

Eq. (23) is a one-dimensional propagation equation. The term on the left hand side is the partial time derivative of the acoustic pressure. The terms on the right hand side are attenuation, nonlinearity, and dispersion, respectively. By using the Fourier-Galkerin spectral method, we solve Eqn. (23) in the frequency domain while marching the acoustic pressure along the rays (propagation paths predicted by ray tracing method). Our final propagation equation is

$$\frac{\partial \tilde{p}}{\partial t} = -\Gamma \tilde{p} + i \frac{K}{2} B (\tilde{p})^2, \tag{25}$$

where $\tilde{p}$ is the pressure in frequency domain. We assemble attenuation and dispersion terms. The combined coefficient Γ is

$$\Gamma = \delta K^2 q^2 + iKq \sum_\zeta \frac{(\Delta c_\zeta)}{1 - iKq\tau_\zeta c}, \tag{26}$$

where the q is the Fourier transfer coefficient for different frequencies and the τ_ζ represents the relaxation time for different components. The generalized Burgers' equation is applied to the ray path with path-dependent attenuation and dispersion coefficients obtained from the Sutherland and Bass [26] model. To introduce turbulent scattering into the generalized Burgers' equation, we

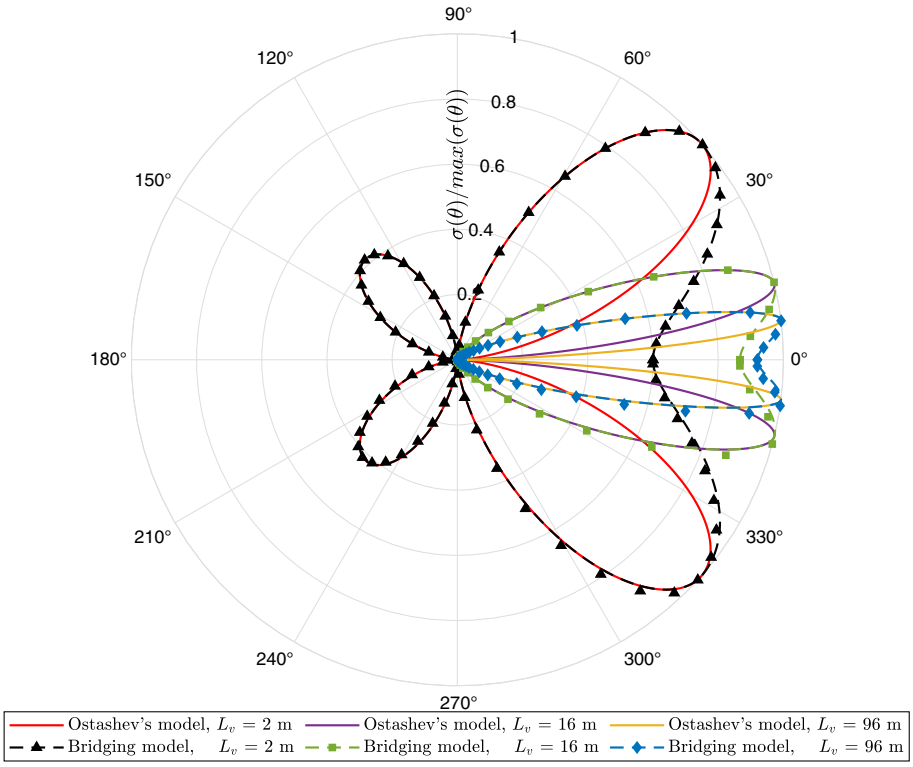

Fig. 2. An example of the bridging cross-section model compared with Ostashev's model.

modified the coefficient Γ with the newly-developed turbulent attenuation coefficient α_t from the previous subsection. Thus, the newly combined coefficient is

$$\Gamma_t = \delta K^2 q^2 + iKq \sum_{\zeta} \frac{(\Delta c_\zeta)}{1 - iKq\tau_\zeta c} + \alpha_t. \tag{27}$$

Finally, we obtain our governing equation for the propagation as

$$\frac{\partial \tilde{p}}{\partial t} = -\Gamma_t \tilde{p} + i\frac{K}{2} B(\tilde{p})^2, \tag{28}$$

which is capable of capturing the effects of nonlinearity, turbulent attenuation, and atmospheric absorption and dispersion.

3. Wind Tunnel Experiments Validation

A series of boundary layer wind tunnel propagation experiments were conducted in the UFBLWT to validate the turbulent attenuation coefficient developed in the previous section. The detailed experimental procedure and calibration of the UFBLWT propagation experiments were recently published by Zhang et al. [27]. The experimental data was made publicly available through the DesignSafe cyberinfrastructure by Zhang et al. [28]. In this section, we introduce the setup, discuss steps of the test procedure, and discuss the results of the experiments. Then the validation of the turbulent attenuation coefficient is presented via comparisons of our predictions with our measurements.

3.1. UFBLWT Experiments Setup

Three objectives of the experiment are critical for model validation. The first involves careful construction of the source acoustic signal within the tunnel. The second involves careful measurements and characterization of the turbulence statistics within the tunnel. The third involves measuring the acoustic signal altered by the turbulence.

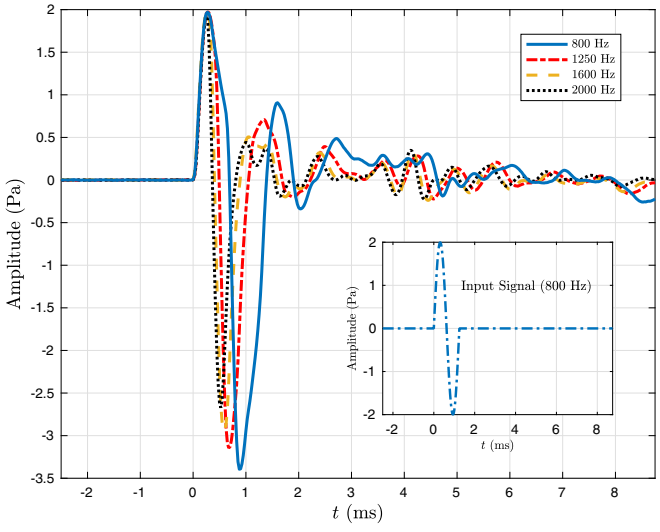

Fig. 3. Output single cycle signals at 2 m from speaker. [27].

The acoustic source signal is synthesized via a small speaker placed within the wind tunnel. Fig. 3 shows 36-ensemble averages of the measured acoustic wave from the source speaker, and these signals are considered as the baseline source signal. The Matlab-generated acoustic source signal of 800 Hz is shown as the blue-dash line in the figure inset. Source signals are created as 800 Hz, 1250 Hz, 1600 Hz, and 2000 Hz pulses. For the first crests of each acoustic source signal, the over-pressure amplitudes are 2 Pa. By comparing with the acoustic source signal's trough, the impulse responses are observed at the troughs for all four signals since the amplitudes of the troughs are −3.393 Pa, −3.136 Pa, −2.857

Pa, and −2.657 Pa for 800 Hz, 1250 Hz, 1600 Hz, and 2000 Hz, respectively [27]. The 800 Hz pulse has the most intense response since its trough has the highest magnitude of 3.393 Pa.

Turbulence statistics are measured within the tunnel using a high-frequency Cobra probe that is mounted on a mechatronic gantry system. Via this approach, both mean flow and turbulence statistics are measured through the turbulent boundary layer. Probes are moved downstream and in the cross-stream direction at multiple locations. Boundary layer roughness is varied via individually computer-controlled roughness elements. In this way, our predictions and experiments encompass a wide range of realistic atmospheric conditions with varying turbulence statistics, ground roughness, and mean flow velocities.

Finally, we measure the turbulent-distorted acoustic signal, which is obtained by a G.R.A.S. [29] microphone system. Temperature, humidity, static pressure, and turbulence measurements are available to the reader via DesignSafe [28].

The experimental setup is shown in Fig. 4. The source signal is generated by a speaker located near the inlet of the wind tunnel, and the microphone is located near the wind tunnel exit. The x coordinate is aligned with the ground center line of the tunnel, and the z direction points to the ceiling. The total propagation distance is 22 m for the acoustic tests. Both the microphone and speaker have adjustable height so that their elevation height (EL) can vary. The meanflow and turbulence measurement system is not present during acoustic tests, so that they do not scatter the acoustic wave. We set the ground element height (EH) at the identical height to the floor and identical angle to the flow.

Reflections of the source signal on the tunnel walls and the background tunnel noise reduce the quality of our measurements. To reduce these effects, we implemented an ensemble averaging technique and a linear reflection wave prediction to reduce and remove these disturbances, respectively. By taking the ensemble average of the 36 repeated single cycles for each frequency, the broadband turbulent noise can be efficiently removed, and the signal-to-noise ratio is improved to 8.9 dB and higher for acoustic measurements. We isolated the portion of the received signal that resulted from reflection from the tunnel walls by combining the single-cycle signal design and linear wave propagation prediction. The time delay between the incident wave and reflected wave allows us to use linear acoustic theory to remove the reflected waves. The reflection surfaces are the ceiling, two sidewalls, and the ground. The ceiling and side walls are made of painted plywood, and the ground is made of phenolic plywood. For the ceiling and sidewalls of the tunnel, the surfaces are considered as reflective boundaries since the acoustic impedance is 1.5×10^6 Pa · s/m, which is much larger than the air's acoustic impedance (approximately 400 Pa · s/m) [30]. For the ground reflection, the angle of incidence is between 85.3 to 89.1 degrees (varying due to increasing EL), which causes a grazing [31] effect. Thus, the ground reflection is not included due to the roughness elements, which scatter the incident wave and prevent its energy from reaching the microphone.

3.2. Predictions Compared to UFBLWT Measurements

Here, we present our predictions and compare them with our wind tunnel measurements. Tunnel measurements of velocities, turbulent kinetic energy (TKE), and length scales are used directly within the propagation solver. Fig. 5 shows four example comparisons from the UFBLWT. The black lines are the experimental measurements, the dash-dot red lines are the predictions from the nonlinear propagation solver, the blue dot lines are the results of the linear wave prediction, and the bars represent the uncertainty of the experiment. To emphasize the time of arrival of reflected waves, we have placed vertical dashed blue lines. The detailed EH, EL, TKE, and L_v of 24 validation cases are listed in the Table 1. Tests 1, 2, and 3 are measured at the same EL of 170 mm with the mean wind speed of 5.16 m/s, 6.86 m/s, and 8.64 m/s, while Test 10 is measured at the EL of 900 mm with the wind speed of 5.16 m/s. The EH of these four cases is set at 30 mm. More cases are accessible via the DesignSafe data depot [28]. The linear wave prediction successfully captures the reflections as the waveform of the prediction matches the experimental data. From the experimental results in Test 10, we can clearly see that the ceiling reflected wave created a 0.36 Pa crest at + 1.2 ms, along with the impulse response (crest at + 0.85 ms) of the test signal. The two sidewalls reflected waves produce another crest at + 2.4 ms of 0.4 Pa, which doubles the amplitude compared with the direct wave at $t = 0$.

The source signals are those shown in Fig. 3. Predictions are shown in Fig. 5 and are compared with the ensemble-averaged measurement without reflections. The solver captures the turbulent attenuation effect as the predicted amplitudes of the first crest in Test 1, 2, and 3 are 0.18 Pa, 0.11 Pa, and 0.09 Pa, which are all located in the uncertainty range of the experimental results. A 0.09 Pa amplitude decrease is observed with increasing mean TKE from 0.27 m^2/s^2 to 0.75 m^2/s^2. The turbulent length scale of Test 1 and Test 10 are 1.89 m and 2.06 m, respectively, while the TKE of Test 1 and Test 10 are 0.27 m^2/s^2 and 0.18 m^2/s^2. The decrease in TKE and increase in length scale cause a 0.005 Pa amplitude increase from Test 1 to Test 10.

Errors of the 24 predictions relative to experiments are shown in Fig. 6. The black bar represents 95% uncertainty of the experimental data. The dots represent the percentage error between the prediction and experiment, and the outliers (predictions not located within the uncertainty band) are colored as red dots and labeled by their test number. The average error of Oshtashev's model is 24.32%, and the average error of the Bridging model is 22.45%. By removing the outliers from the results, the error of

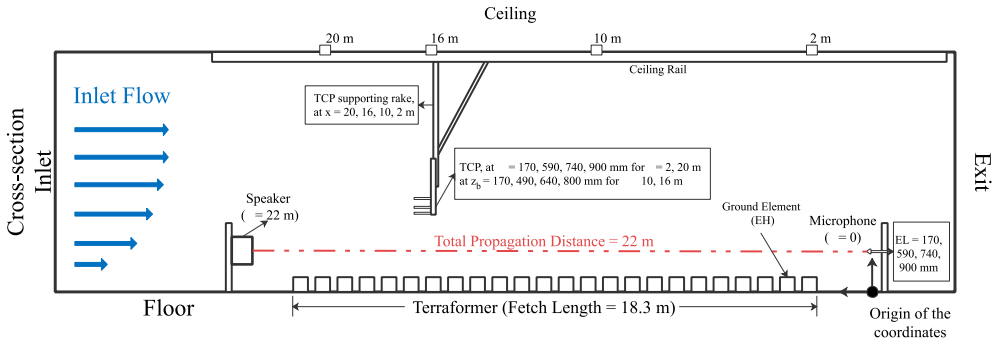

Fig. 4. Experimental schematic from the UFBLWT acoustic propagation tests [28].

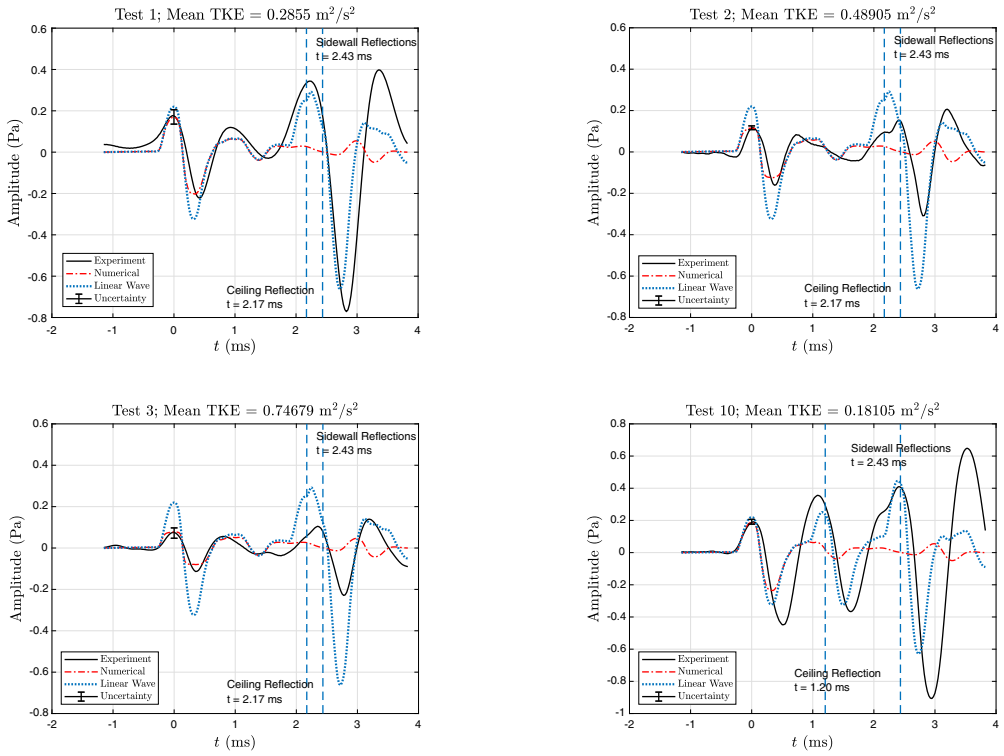

Fig. 5. Comparison between predictions and wind tunnel measurements.

Table 1
The case list for the UFBLWT validation.

Test	*EH* (mm)	*EL* (mm)	TKE (m^2/s^2)	L_v (m)	Test	*EH* (mm)	*EL* (mm)	TKE (m^2/s^2)	L_v (m)
1	0	170	0.29	1.89	13	30	170	0.35	1.78
2	0	170	0.49	2.55	14	30	170	0.64	2.40
3	0	170	0.75	3.17	15	30	170	0.96	2.98
4	0	590	0.25	2.00	16	30	590	0.27	2.01
5	0	590	0.47	2.70	17	30	590	0.51	2.70
6	0	590	0.67	3.38	18	30	590	0.68	3.40
7	0	740	0.23	2.04	19	30	740	0.23	2.05
8	0	740	0.40	2.76	20	30	740	0.41	2.78
9	0	740	0.56	3.42	21	30	740	0.60	3.44
10	0	900	0.18	2.06	22	30	900	0.19	2.08
11	0	900	0.32	2.80	23	30	900	0.33	2.81
12	0	900	0.47	3.48	24	30	900	0.47	3.49

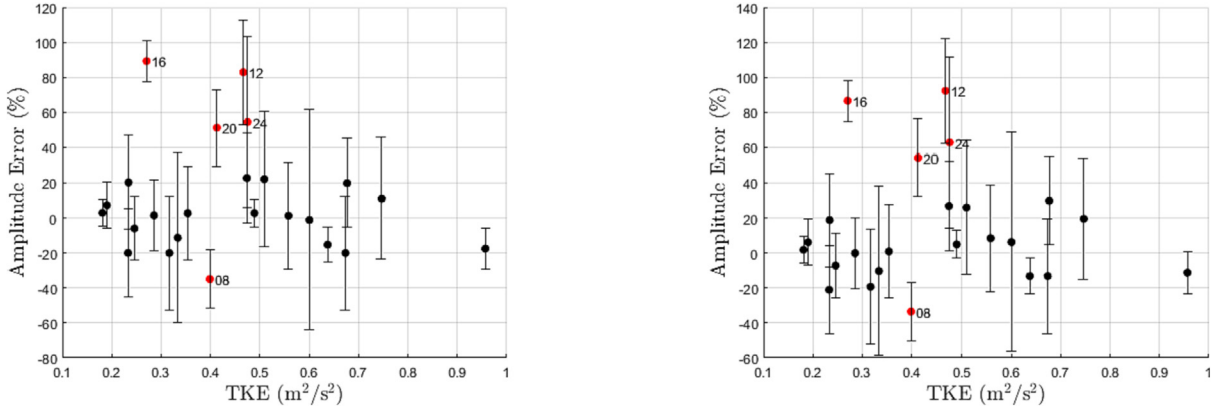

Fig. 6. The error comparison between the bridging model (a) and Ostashev's model (b).

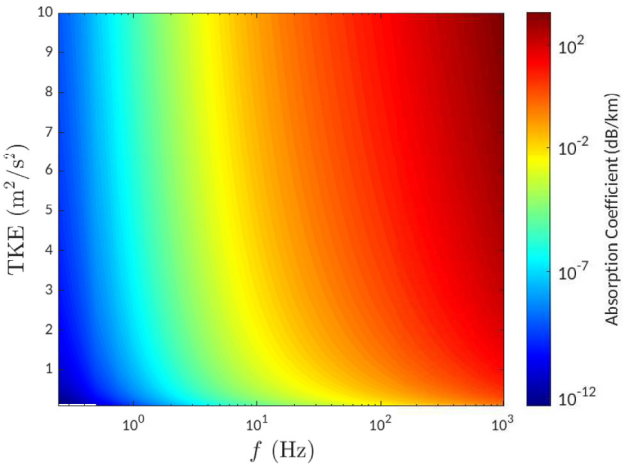

Fig. 7. Absorption coefficient with respect to TKE and acoustic frequency.

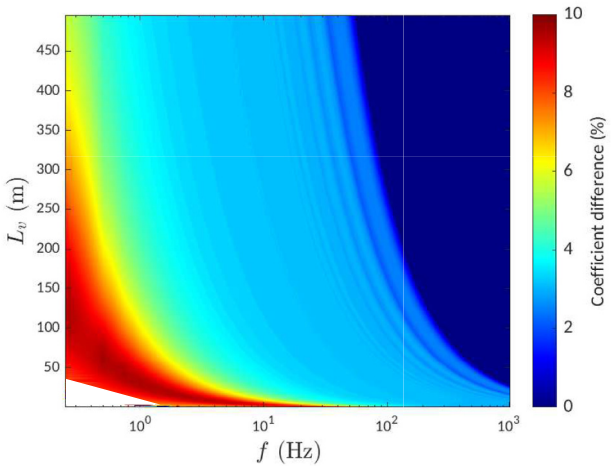

Fig. 9. Turbulent attenuation coefficient difference between the bridging model and Ostashev's model.

Ostashev's model decreases to 12.67%, while the bridging model's error is 11.9%. Turbulent attenuation is observed in the experimental results and is captured by the propagation solver. We note that our predictions and experiments are dimensional, one-to-one, and involve inhomogeneous turbulence.

4. Numerical Model Analysis and Parametric Study of the Propagation Solver

We numerically investigate more realistic acoustic propagation scenarios with the new bridging model to understand the model's behavior. In particular, we examine TKE and L_v's effects on the propagation and quantify their effect on the absorption coefficient α_t. Fig. 7 shows the distribution of α_t with frequency range of 0.25 Hz to 1024 Hz and TKE range from 0.1 to 10 m^2/s^2. In Fig. 7, the x-axis is the acoustic frequency in Hz, the y-axis is the TKE in m^2/s^2, and the colors represent the value of the turbulent absorption coefficient. The integral length scale L_v for this prediction is fixed at 1.2 m. The coefficient contours are in log scale ranging from 10^{-15} to 1 dB/km. The overall trend of α_t is increasing with increasing TKE, as expected. Turbulent absorption shows a linear increase with frequency, which is similar to the trend involving the atmospheric absorption coefficient of Sutherland and Bass [26].

The distribution of the turbulent absorption coefficient α_t in the frequency-L_v domain is presented in Fig. 8. Unlike Fig. 7, the x-axis is linear to illustrate a clearer insight into the dependency between the L_v and α_t. The TKE for this prediction is set at 0.2 m^2/s^2. The L_v's range is from 0.5 to 500 m, while the frequency range is kept the same as in Fig. 7. By using the linear x-axis, the α_t's profile for high frequency shows a hill-like shape with increasing L_v. The L_v of the turning point of these hill-like profiles decreases with increasing frequency. This behavior is caused by the integration of Eqn. 18, where L_v can alter the integrating area in wavenumber space. Therefore, the correlation between L_v and acoustic frequency contributes to the curve in Fig. 8. Similar behavior is also observed in the predictions of Ostashev's model, and the predicted coefficient difference between these two models is shown in Fig. 9. Here, the turbulence statistics are identical to those presented in Fig. 8, and the difference is normalized by the Ostashev's model prediction. At $f > 1000$ Hz, the difference between these two models is negligible. For the frequency at 20 Hz, the difference approaches 3% to 4% with varying L_v. The maximum difference (about 10%) appears from f at 10 Hz and L_v at 0.5 m to f = 0.25 Hz and L_v at 100 m. This indicates that the effect of the bridging model is more apparent at low frequencies. For the frequency higher than 1000 Hz, there is no obvious difference between the bridging model and Ostashev's model. Thus, we consider our model's maximum acoustic frequency as 1000 Hz. For acoustic frequencies lower than 1 Hz, the effect of acoustic gravity waves must be accounted for. Since our model is not capable of physically capturing the acoustic gravity wave, we set our lowest acoustic frequency as 1 Hz and only simulate scattering attenuation for altitudes lower than 20 km.

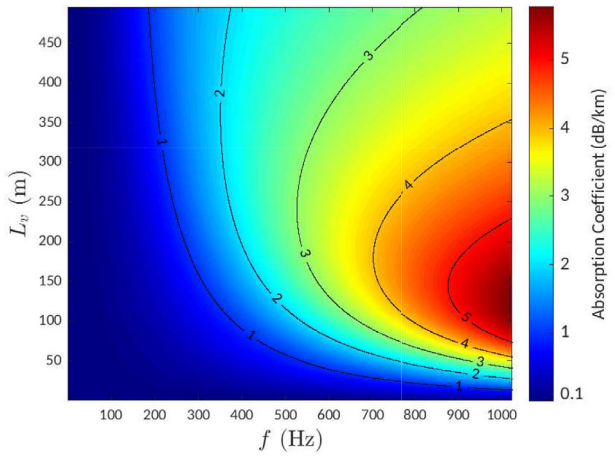

Fig. 8. Absorption coefficient as a function of turbulent length scale and frequency.

We implemented the turbulent scattering attenuation coefficient into the generalized Burgers' equation for the numerical propagation tests. Two broadband test signals are selected and propagated along a horizontally straight-line path at the altitude of 100 m for a distance of 50 km. The turbulence of this altitude is generated by the atmospheric turbulent model developed by Lukin [32], which provides the TKE and integral length scale at altitude, which are 0.6 m^2/s^2 and 12 m, respectively. Two signals we employed for the propagation solver are the broadband tornadic infrasound signal and a shock wave signal. Fig. 10 shows the spectra of the shock wave with and without turbulent effects. In this figure, the source signal is a left-running "N" wave. The pressure time history of the source signal is shown in the left-bottom corner in Fig. 10 with an amplitude of 2 Pascal and a total time span of 1 s. The spectrum of the source signal is shown as the black solid line (represented by (a)), while the spectra of received signals are

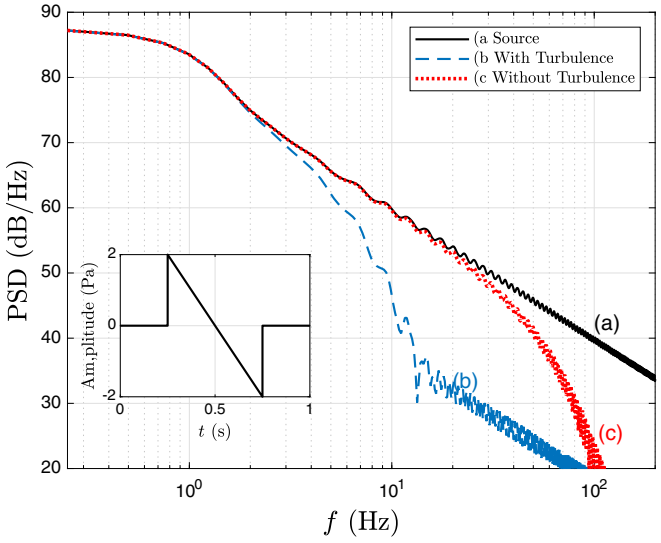

Fig. 10. Spectra of the shock wave propagation case.

represented by the blue dash line (b) and red dot line (c) for propagation with and without turbulent effect, respectively. For the low-frequency region from 0.25 to 2 Hz, the attenuation effects are negligible for both atmospheric attenuation and turbulent attenuation. The turbulent attenuation appears at the frequency of 2 Hz, where the PSD drop is about 0.22 dB. For the frequency region higher than 20 Hz, the propagation solver loses its fidelity, and the PSD is below 30 dB for the turbulent-altered signal. By comparing with the spectrum without turbulence, the turbulent-induced PSD drop is higher than 25 dB at 20 Hz. The atmospheric attenuation obtains influence on the spectrum with the frequency higher than 10 Hz, as shown by the red-dot line. The high-frequency (larger than 100 Hz) energy of the shock wave is discharged significantly by the atmospheric attenuation with the PSD lower than 20 dB. In the shock wave propagation case, the turbulent attenuation for the low-frequency region from 2 Hz to 20 Hz is significantly higher than the atmospheric attenuation. Because of the positive correlation between the attenuation and frequency, the turbulent effect on the N-wave is a "rounding" effect like atmospheric attenuation, but about five times stronger for this specific

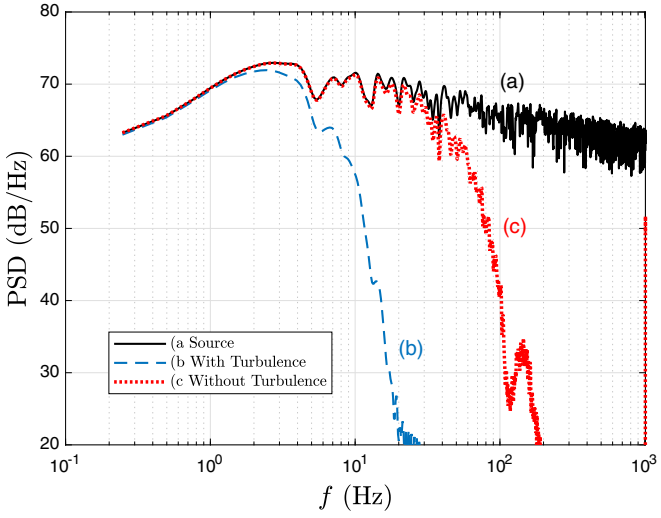

Fig. 11. Spectra of the broadband tornado signal propagation case.

turbulent condition by comparing the frequency-dependent PSD drop.

A broadband tornadic signal propagation case is conducted with the same turbulence statistics to illustrate the approach. The broadband tornadic signal is reconstructed via Frazier et al. [33]'s mathematical model. Fig. 11 shows the results of these propagation cases. The black solid line (a) is the spectrum of the source signal, which is a broadband signal from 0.25 Hz to 1024 Hz. The blue-dash line and the red-dot line are the spectra of the received signals with and without turbulent effects, respectively, following the same manner as Fig. 10. For this case, the turbulent attenuation of 0.25 dB PSD drop is observed at the frequency of 1 Hz, while the atmospheric attenuation causes 0.25 dB PSD drop at 10 Hz. In Fig. 11, we can find the interception points of the 30 dB horizontal line with the blue and red lines located at the frequencies of 15 and 100 Hz, respectively. For the 15 Hz signal, the PSD drop caused by atmospheric attenuation is only around 0.04 dB. Thus, the turbulent attenuation at 15 Hz has a similar intensity as the atmospheric attenuation at 100 Hz.

Fig. 12 shows the results of the OASPL difference with and without turbulence. The ΔOASPL is the difference between the OASPL of the propagation within a turbulent field and without, respectively. For the first test, the TKE of the turbulent model is fixed at 0.0285 m^2/s^2, while the L_v varies from 2.5 to 250 m. A ±5% perturbation is applied to evaluate the sensitivity of the model. As shown in Fig. 12, the effects of L_v on the ΔOASPL are linear, while the effects of the perturbation also follows a linear variation.

We also compared our predictions with the sonic boom propagation study of Lipkens and Blackstock [34]. The experiment modeled sonic boom propagation in a turbulent atmosphere by propagating the electric-sparked *N* waves through a plane jet [34]. Two hundred pressure waveforms were recorded in Lipkens and Blackstock [34]'s experiment, providing an averaged waveform for our statistical model to compare. We reconstructed the source signal based upon their measurements. The statistical result of the experiment is shown in Table 2, where τ is the rise time, Δp is the peak pressure, and T is the sonic boom duration.

The propagation distance (from the spark to the microphone) is 0.45 m, thus we use an *N*-wave with an 800 Pa peak pressure to represent the source signal. Standard atmospheric conditions are applied for the solver to obtain the received waveform without the turbulent scattering model, and the numerical result is shown in Fig. 13 as the solid red waveform. In Fig. 13, the blue dot-dash waveform is the received signal with turbulent effects, and the black dash line is the reconstructed source signal (spark generated *N* wave).

The TKE is set to 2.576 m^2/s^2 based on the rms velocity fluctuation of 2.27 m/s measured in the experiment. The measured integral length scale is in the range of 0.01 m to 0.08 m in the experiment, and we use 0.01 m for our numerical simulation. We present both pressure–time history (a) and spectrum (b) of the numerical results in Fig. 13. The peak pressure of the non-turbulent result is 643.4 Pa, which is 1.2% lower than the experimental data. The difference is likely due to the unknown waveform of the source signal. For the received signal with turbulent effects, the peak pressure is 595.2 Pa. Thus, a 7.5% peak pressure drop is observed in our numerical simulation, compared to the 4.8% peak pressure decrease in the experiment. The rise time of the numerical results increases from 2.01 μs to 2.81 μs, while the rise time in experimental data increases from 0.506 μs to 1.45 μs. The spectra of the waveforms are also presented in Fig. 13(b). For the waveform without turbulent effects, we observe a broadband PSD reduction for frequencies higher than 1 MHz, which is caused by atmospheric absorption. The spectrum with turbulent effects shows a higher PSD drop for frequencies higher than 2 MHz. For

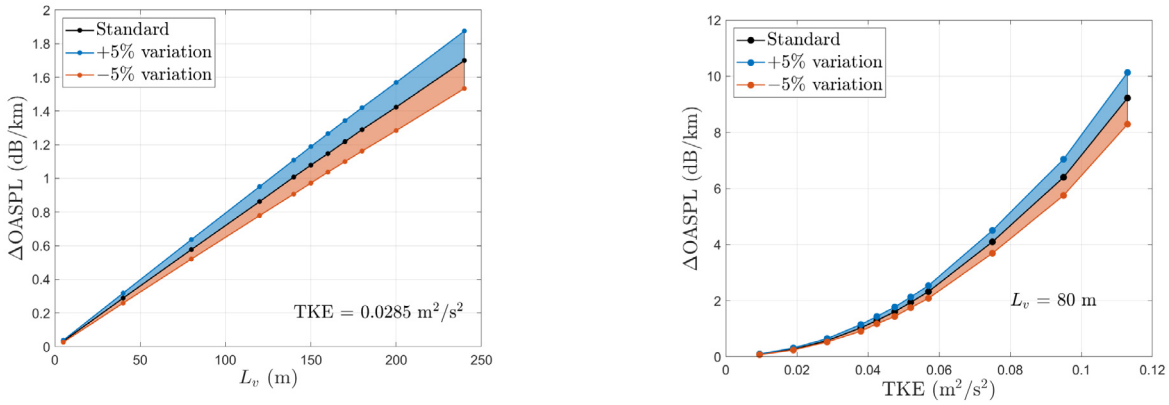

Fig. 12. ΔOASPL of the bridging model for tornadic broadband signal propagation.

Table 2
Statistical results of the plane *N* waves in [34].

	τ (μs)		Δ p (Pa)		T (μs)	
	mean	σ	mean	σ	mean	σ
no turb.	0.506	0.010	651.4	6.0	10.642	0.191
turb.	1.450	1.450	620.7	228.4	11.317	1.286

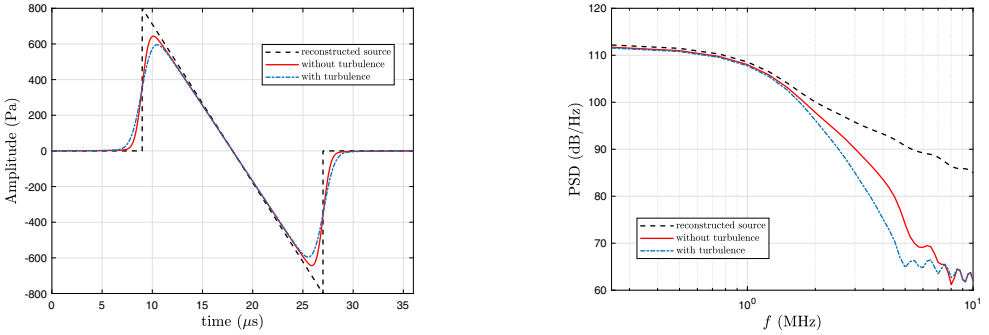

(a) pressure-time history (b) spectrum

Fig. 13. Comparison with the experimental results of Lipkens and Blackstock [34] .

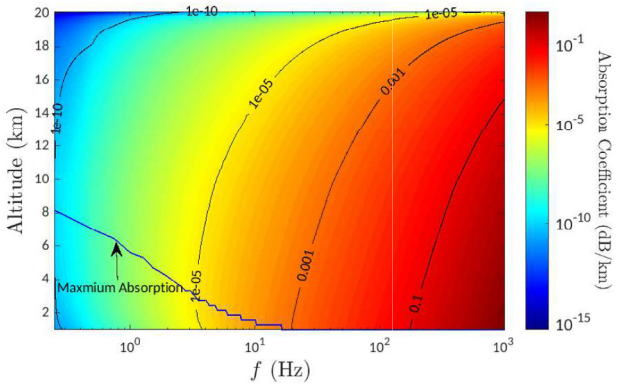

Fig. 14. Absorption coefficient distribution in frequency and altitude domain.

example, a 10 dB additional PSD drop is observed at 4 MHz due to turbulent effects. Compared to the experimental data in [34], our numerical results show similar behaviors in peak pressure drop and rise time increase.

Finally, we examine an atmosphere with varying TKE and L_v. Variations are governed by the model of Lukin [32] in an altitude range from 0 to 20 km. Fig. 14 shows one representative example of the turbulent attenuation distribution from 0 to 20 km. The dark blue line represents the maximum absorption and also represents the height of maximum absorption for each frequency. The dependency of the absorption coefficient relative to frequency is clearly observed as the overall trend of the coefficient increases from 10^{-10} dB/km to 10^{-1} dB/km with increasing frequency from 0.2 to 1000 Hz at 2 km altitude. For $f > 20$ Hz, the absorption decreases with increasing altitude monotonically. Also, α_t decreases with increasing altitude monotonically. This is due to the combined effect of increasing L_v and decreasing TKE as altitude increases. For infrasound frequencies (less than 20 Hz), the maximum turbulent absorption altitude increases with decreasing frequency, and this maximum occurs near 8 km at 0.25 Hz.

5. Summary and Conclusion

In this paper, a bridging model of acoustic-turbulent interaction for long-range propagation is introduced. A characteristic

turbulent wave number, k_l, represents the turbulent integral length scale. For scattering wavenumbers larger than k_l, the bridging model converges to Ostashev's scattering model. For scattering wavenumbers smaller than k_l, the refraction model replaces the scattering model. The refracted cross-section σ_r is expressed by σ_v, L_v, and partial integration of the turbulence spectrum $E(k)$. A sine function bridges the refraction model and scattering model by matching its maximum value to the maximum cross-section.

A series of wind tunnel propagation experiments are conducted in the NSF UFBLWT to validate the newly developed bridging model. The experiments successfully captured the turbulent attenuation. The peak amplitude of the received signal varies from 0.22 Pa to 0.084 Pa, with the mean wind tunnel speed from 0 to 8.56 m/s. These results showed that both Ostashev's and the new model make excellent predictions. The new model successfully accounts for inhomogeneous turbulent boundary layers with rough terrains.

A series of numerical studies are conducted to investigate the new model's characteristics and its influence on the propagation of signals. The TKE and L_v's effects on predictions are presented, where the TKE primarily affects the magnitude of α_t, and L_v alters α_t distribution in frequency. The OASPL of the received tornadic signal is used to analyze the overall influence of the bridging model. Both TKE and L_v contribute to a larger decrease in OASPL. By implementing a realistic turbulent atmospheric model with the bridging model, a maximum absorption line is observed within the α_t contour.

CRediT authorship contribution statement

Tianshu Zhang: Methodology, Data curation, Writing - original draft. **Steven A.E. Miller:** Conceptualization, Investigation, Supervision, Writing - review & editing.

Data availability

Data has been published on DesignSafe CI

Declaration of Competing Interest

The authors declare the following financial interests/personal relationships which may be considered as potential competing interests: Steven A. E. Miller reports financial support was provided by National Oceanic and Atmospheric Administration.

Acknowledgements

These models are inspired by the scattering model of Ostashev and Wilson and the bridging function of Blackstock. This program was supported by the NOAA Weather and Air Quality Research program award number NA18OAR4590306.

References

[1] Pierce AD. Acoustics: An Introduction to its Physical Principles and Applications. Springer Verlag; 2019.
[2] Pichon AL, Blanc E, Hauchecorne A. Infrasound Monitoring for Atmospheric Studies. Netherlands: Springer; 2009. 10.1007/978-1-4020-9508-5.
[3] Ostashev VE, Wilson DK. Acoustics in moving inhomogeneous media. CRC Press; 2015.
[4] Kuznetsov V. Equations of nonlinear acoustics. Sov Phys Acoust 1971;16:467–70.
[5] Zabolotskaya E, Khokhlov R. Quasi-plane waves in the nonlinear acoustics of confined beams. Sov Phys Acoust 1969;15:35–40.
[6] Blanc-Benon P, Lipkens B, Dallois L, Hamilton MF, Blackstock DT. Propagation of finite amplitude sound through turbulence: Modeling with geometrical acoustics and the parabolic approximation. J Acoust Soc Am 2002;111:487–98. https://doi.org/10.1121/1.1404378.
[7] Lipkens B. Model experiment to study sonic boom propagation through turbulence. part III: Validation of sonic boom propagation models. J Acoust Soc Am 2002;111:509–19. https://doi.org/10.1121/1.1371974. DOI: 10.1121/1.1371974.
[8] Pierce AD. Statistical theory of atmospheric turbulence effects on sonic-boom rise times. J Acoust Soc Am 1971;49:906–24.
[9] Piacsek AA. Atmospheric turbulence conditions leading to focused and folded sonic boom wave fronts. J Acoust Soc Am 2002;111:520–9.
[10] Stout TA, Blanc-benon P, Reichard K. Simulation of N-Wave and Shaped Supersonic Signature Turbulent Variations Ph.D. thesis. Pennsylvania State University; 2018.
[11] J. Rathsam, A Study in a New Test Facility on Indoor Annoyance Caused by Sonic Booms, Technical Report NASA/TM-2012-217332, L-20108, NF1676L-14072, 2012.
[12] Goldreich P, Kumar P. The interaction of acoustic radiation with turbulence. Astrophys J 1988;326:462–78.
[13] Brown EH, Clifford S. On the attenuation of sound by turbulence. J Acoust Soc Am 1976;60:788–94.
[14] Lighthill MJ. On the energy scattered from the interaction of turbulence with sound or shock waves. Mathematical Proceedings of the Cambridge Philosophical Society 1953;49:531–51. https://doi.org/10.1017/s0305004100028693.
[15] Tatarski VI. Wave Propagation in a Turbulent Medium. Dover Publication; 1967.
[16] Muhsin M, Sunilkumar S, Ratnam MV, Parameswaran K, Mohankumar K, Mahadevan S, Murugadass K, Muraleedharan P, Kumar BS, Nagendra N, Emmanuel M, Chandran P, Koushik N, Ramkumar G, Murthy B. contrasting features of tropospheric turbulence over the indian peninsula. J Atmos Solar Terr Phys 2020;197:. https://doi.org/10.1016/j.jastp.2019.105179105179.
[17] Candel SM. Numerical Solution of Conservation Equations Arising in Linear Wave Theory: Application to Aeroacoustics. J Fluid Mech 1977;83:465–93. https://doi.org/10.1017/S0022112077001293.
[18] Blackstock DT. Generalized burgers equation for plane waves. J Acoust Soc Am 1985;77:2050–3. https://doi.org/10.1121/1.391778.
[19] Scott J, Blanc-Benon P, Gainville O. Weakly nonlinear propagation of small-wavelength, impulsive acoustic waves in a general atmosphere. Wave Motion 2017;72:41–61. https://doi.org/10.1016/j.wavemoti.2016.12.005.
[20] Scott J, Blanc-Benon P, Gainville O. Weakly nonlinear propagation of small-wavelength, impulsive acoustic waves in a general atmosphere. Wave Motion 2017;72:41–61. https://doi.org/10.1016/j.wavemoti.2016.12.005.
[21] Gainville O. Modeling of Atmospheric Propagation of Infrasound Waves by the Method of Nonlinear Ray Tracing Ph.D. thesis. Ecole Centrale de Lyon 2008.
[22] Tennekes H, Lumley JL. A first course in turbulence. MIT press; 2018.
[23] Sreenivasan KR. An update on the energy dissipation rate in isotropic turbulence. Phys Fluids 1998;10:528–9. https://doi.org/10.1063/1.869575.
[24] Blackstock DT. Connection between the fay and fubini solutions for plane sound waves of finite amplitude. J Acoust Soc Am 1966;39:1019–26.
[25] Blackstock DT, Fundamentals of physical acoustics, 2001.
[26] Sutherland LC, Bass HE. Atmospheric Absorption in the Atmosphere up to 160 km. J Acoust Soc Am 2004;115:1012–32. https://doi.org/10.1121/1.1631937.
[27] Zhang T, Ojeda-Tuz MA, Gurley KR, Miller SAE. Experiments in a large boundary layer wind tunnel: Propagation of noise through the turbulent boundary layer. J Struct Eng 2022;148. https://doi.org/10.1061/(asce)st.1943-541x.0003275.
[28] Zhang T, Ojeda M, Miller S, Gurley K, Acoustic propagation experiments in a turbulent atmosphere, volume 1 of Prediction of Long-Range Infrasound Propagation from Tornadoes Based on New Atmospheric Boundary Layer Wind Tunnel Experiments, Designsafe-CI, 2021. 10.17603/DS2-BPAV-8W29.
[29] Sound GRAS, Vibration GRAS. 46AZ 1/2" CCP Free-field Standard Microphone Set, Low Frequency, G.R.A.S. Sound Vibration 2015.
[30] Putramulyo S, Wirawan R, Alaa S, Qomariyah N. The analysis of attenuation coefficient and acoustic impedance of ceiling panel using impedance chamber method. Indonesian Phys Rev 2018:32–41. 10.29303/ipr.v1i1.7.
[31] Taylor ME. Grazing rays and reflection of singularities of solutions to wave equations. Commun Pure Appl Math 1976;29:1–38.
[32] Lukin V. In: Vernin J, Benkhaldoun Z, Muñoz-Tuñón C, editors. Astronomical Site Evaluation in the Visible and Radio Range of Astronomical Society of the Pacific Conference Series, volume 266. p. 18.
[33] Frazier WG, Talmadge C, Park J, Waxler R, Assink J. Acoustic detection, tracking, and characterization of three tornadoes. J Acoust Soc Am 2014;135:1742–51. https://doi.org/10.1121/1.4867365.
[34] Lipkens B, Blackstock DT. Model experiment to study sonic boom propagation through turbulence. part i: General results. J Acoust Soc Am 1998;103:148–58. https://doi.org/10.1121/1.421114.